

# Monolithic Silicon Photonic Architecture for Training Deep Neural Networks with Direct Feedback Alignment

Matthew J. Filipovich,<sup>1,\*</sup> Zhimu Guo,<sup>1</sup> Mohammed Al-Qadasi,<sup>2</sup> Bicky A. Marquez,<sup>1</sup> Hugh D. Morison,<sup>1</sup> Volker J. Sorger,<sup>3</sup> Paul R. Prucnal,<sup>4</sup> Sudip Shekhar,<sup>2</sup> and Bhavin J. Shastri<sup>1,5</sup>

<sup>1</sup>*Department of Physics, Engineering Physics and Astronomy,  
Queen's University, Kingston, ON K7L 3N6, Canada*

<sup>2</sup>*Department of Electrical and Computer Engineering,  
University of British Columbia, Vancouver, BC V6T 1Z4, Canada*

<sup>3</sup>*Department of Electrical and Computer Engineering,  
George Washington University, Washington, DC 20052, USA*

<sup>4</sup>*Department of Electrical Engineering, Princeton University, Princeton, NJ 08542, USA*

<sup>5</sup>*Vector Institute, Toronto, ON M5G 1M1, Canada*

The field of artificial intelligence (AI) has witnessed tremendous growth in recent years, however some of the most pressing challenges for the continued development of AI systems are the fundamental bandwidth, energy efficiency, and speed limitations faced by electronic computer architectures. There has been growing interest in using photonic processors for performing neural network inference operations, however these networks are currently trained using standard digital electronics. Here, we propose on-chip training of neural networks enabled by a CMOS-compatible silicon photonic architecture to harness the potential for massively parallel, efficient, and fast data operations. Our scheme employs the direct feedback alignment training algorithm, which trains neural networks using error feedback rather than error backpropagation, and can operate at speeds of trillions of multiply-accumulate (MAC) operations per second while consuming less than one picojoule per MAC operation. The photonic architecture exploits parallelized matrix-vector multiplications using arrays of microring resonators for processing multi-channel analog signals along single waveguide buses to calculate the gradient vector of each neural network layer in situ, which is the most computationally expensive operation performed during the backward pass. We also experimentally demonstrate training a deep neural network with the MNIST dataset using on-chip MAC operation results. Our novel approach for efficient, ultra-fast neural network training showcases photonics as a promising platform for executing AI applications.

## INTRODUCTION

Propelled by recent advances in deep learning,<sup>1</sup> the fields of artificial intelligence (AI) and neuromorphic computing (neuro-biological computer architectures) have seen a renaissance over the past decade.<sup>2</sup> Today, the software implementations of AI algorithms are executed on traditional computers based on the von Neumann architecture.<sup>3</sup> However, this architecture faces inherent data-transfer speed limitations due to the separation of memory and processor unit, known as the von Neumann bottleneck. Neuromorphic computing seeks to eliminate this constraint by exploiting the underlying elementary physics of hardware systems to create an isomorphism with AI algorithms.<sup>4</sup> With the ultimate limit of Moore's law, which claims that the number of transistors on a microchip doubles every two years, approaching saturation and the exponentially increasing needs from advanced machine learning algorithms,<sup>5,6</sup> neuromorphic computing has attracted renewed interest as an alternative to the standard electronic digital computer architectures.<sup>7</sup>

Silicon photonics has shown to be a promising platform for developing neuromorphic systems due to its compatibility with the mature silicon integrated circuit industry and the availability of high-quality silicon-on-insulator (SOI) wafers.<sup>8,9</sup> Monolithic silicon photonics enables the integration of active photonic and electronic components onto a single photonic integrated chip (PIC), including modulators, detectors, amplifiers, complementary metal-oxide-semiconductor (CMOS) control circuits, and optical multiplexers.<sup>10</sup> Compared to their electronic counterparts for neuromorphic applications, photonic systems offer low latency, high bandwidth density and baud rates, low-cost communication, and inherent parallelism using optical multiplexing.<sup>11,12</sup>

One area of machine learning that would particularly benefit from the low power consumption and high information processing bandwidth enabled by photonics is the training of large neural networks. Several photonic architectures have been proposed for executing in-memory computation of neural network inference.<sup>13–16</sup> However, for the neural network to perform a useful task, the optimal network parameters (weights and biases) must first be determined using

---

\* [matthew.filipovich@queensu.ca](mailto:matthew.filipovich@queensu.ca)

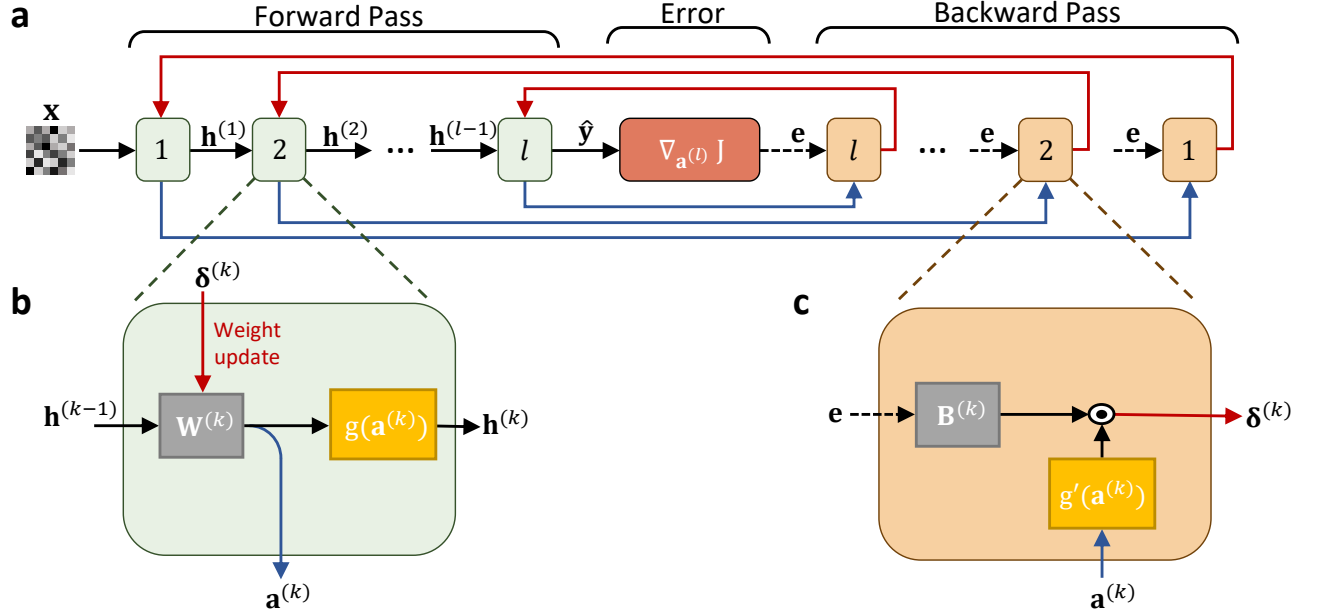


FIG. 1. **Scheme for the DFA algorithm.** (a) The input vector  $\mathbf{x}$  propagates through the neural network with  $l$  layers during the forward pass (inference), where  $\mathbf{h}^{(k)}$  is the output from the hidden layer  $k$  and  $\hat{\mathbf{y}}$  is the output vector. The error vector at the output layer  $\mathbf{e}$ , defined as the gradient of the cost function  $J$ , is calculated and sent directly to each hidden layer. During the backward pass, this error is propagated through fixed random feedback connections for each hidden layer to calculate the gradient vector  $\delta^{(k)}$  which is used for the weight updates. (b) Block diagram of the operations performed during the forward pass at the layer  $k$ . (c) Block diagram of the gradient vector calculations performed during the backward pass at the layer  $k$ .

deep learning training algorithms. These algorithms have high computation and memory costs that pose challenges to the current hardware platforms executing them,<sup>17</sup> and the substantial energy consumption required to train large neural networks using standard von Neumann architectures presents a significant financial and environmental cost.<sup>18</sup> The recently proposed direct feedback alignment (DFA) supervised learning algorithm has gathered interest as a bio-plausible alternative to the popular backpropagation training algorithm.<sup>19</sup> The DFA algorithm, shown in Fig. 1 and further described in the Methods section, is a supervised learning algorithm that propagates the error through fixed random feedback connections directly from the output layer to the hidden layers during the backward pass.<sup>20</sup> Unlike backpropagation, the DFA algorithm does not require the network layers to be updated sequentially during the backward pass, enabling the algorithm to be a suitable candidate for efficient parallelisation using photonics. The training algorithm has been used to train neural networks using the MNIST, Cifar-10, and Cifar-100 datasets, and yields comparable performance to backpropagation.<sup>20</sup> As well, the DFA algorithm has been shown to obtain performances comparable to fine-tuned backpropagation in applications requiring state-of-the-art deep learning networks, including natural language processing and neural view synthesis.<sup>21</sup> A recent theory suggests that training shallow networks with the DFA algorithm occurs in two steps: the first step is an alignment phase where the weights are modified to align the approximate gradient with the true gradient of the loss function, which is followed by a memorisation phase where the model focuses on fitting the data.<sup>22</sup>

Here, we propose a silicon photonic architecture that uses an electro-optic circuit for calculating the gradient vector of each neural network layer *in situ*, which is the most computationally expensive operation performed during the backward pass. The proposed architecture exploits the speed and energy advantages of photonics to determine the gradient vector of each neural network layer in a single operational cycle. The scope of this paper is limited to the implementation of the DFA algorithm's backward pass; however, inference can also be performed using a similar photonic architecture.<sup>13</sup> Training a hardware-based neural network *in situ* could also inherently account for the manufacturing imperfections and variations of the physical neurons. During the backward pass, the error from the network's inference step is encoded on multi-channel optical inputs. The electro-optic circuit then calculates the gradient vector for each hidden layer, which is used to update the network parameters stored in memory using an external digital control system. We also demonstrate training a feed-forward neural network on the MNIST dataset using experimental on-chip results to validate our proposed architecture.

## RESULTS

### Multiply-accumulate operations in photonics

The proposed architecture uses microring resonators (MRRs), which are closed-loop waveguides that use codirectional evanescent coupling between the ring and adjacent bus waveguides, as tunable filters to weight photonic signals through amplitude modulation.<sup>23</sup> By exploiting the plasma dispersion effect, the refractive index of each MRR is adjusted by varying the concentration of carriers through external biasing. This change in refractive index is used to tune the MRR's resonance peaks and modulate the transmission of optical signals for a specified wavelength.<sup>24</sup> In our proposed architecture, the MRRs which perform multiply-accumulate (MAC) operations are arranged in add-drop geometries coupled to two waveguide buses, known as the through and drop ports, as shown in Fig. 2a. Tuning the MRR's resonance to control the amount of light transmission through the two ports effectively weights the input optical signal, a technique which can be exploited to perform the dot product between two vectors.

The dot product operation, which consists of a series of MAC operations  $\mathbf{x} \cdot \mathbf{w} = \sum x_i w_i$ , is executed in photonics using an array of MRRs and a balanced photodetector.<sup>25</sup> Using wavelength-division multiplexing (WDM) techniques to process multi-channel analog signals along the same waveguide bus, where each optical signal with wavelength  $\lambda_i$  is amplitude encoded with a value  $x_i$ , each MRR in the array is tuned with a specified weighting value  $w_i \in [-1, 1]$  for the corresponding optical input wavelength  $\lambda_i$ . The through and drop port transmission spectrums,  $T_p$  and  $T_d$ , of each MRR as a function of round-trip phase shift are Lorentzian-shaped and centered at the resonance phase with the incoming light. When the coupling losses between the MRR and bus waveguides are negligible, the relationship between the through and drop port transmissions for each MRR is  $T_p = 1 - T_d$ . These two ports are connected into a balanced photodetector which gives an effective transfer function in the electrical domain that is proportional to  $|E_0|^2(T_d - T_p)$ , where  $E_0$  is the amplitude of the input optical signal. Thus, the assigned weighting value  $w_i$  of each MRR is given by  $T_d - T_p$ . Using this scheme, external biasing of the MRR tunes the resonance peak to correspond with the desired weighting for a selected optical wavelength, as shown in Fig. 2b. Finally, the dot product between two vectors of size  $N$  can be executed using an array of  $N$  MRRs that are coupled to the same through and drop ports, as shown in Fig. 2c.

The continuous and multi-channel control of MRR arrays based on feedback control is an ongoing area of research, and a record-high accuracy of 8.5 bits for a single MRR using thermal tuning has recently been observed with negligible inter-channel crosstalk.<sup>26</sup> Due to precision limitations in PIC manufacturing leading to device variance, the relationship between the applied MRR bias and the change in weighting value for a specified optical wavelength must be determined experimentally.<sup>27</sup> The current tuning approach relies on feedforward control to calibrate the MRRs, as well as feedback control for sensing the state of the system and correcting for any changes due to dynamic variability, such as environment fluctuations.<sup>28</sup>

### Photonic deep learning architecture

In this section, we introduce the proposed photonic architecture for executing the DFA training algorithm. The architecture exploits MAC operations performed in photonics, as discussed in the previous section, to execute matrix-vector multiplications in the analog domain during the backward pass, which are the most computationally expensive operation performed during training. For each training example during the backward pass, the architecture calculates the gradient vector  $\delta^{(k)}$  of the hidden layer  $k$  in a single operational cycle. The gradient vector (see Fig. 3a) is given by

$$\delta^{(k)} = \mathbf{B}^{(k)} \mathbf{e} \odot g'(\mathbf{a}^{(k)}), \quad (1)$$

where  $\mathbf{B}^{(k)}$  is a fixed random weight matrix with appropriate dimensions for the hidden layer  $k$ ,  $\mathbf{e}$  is the error from the gradient of the cost function,  $\odot$  is the Hadamard product (element-wise multiplication operator), and  $g'$  is the derivative of the activation function with respect to  $\mathbf{a}^{(k)}$ , which is the sum of the weighted input signals in the hidden layer  $k$ . The network's weights and biases are then updated using the calculated gradient vector  $\delta^{(k)}$  for each hidden layer  $k$ .

A schematic of the proposed silicon photonic DFA architecture, which can be implemented on a PIC, is shown in Fig. 3b. The DFA architecture requires a digital control system to tune the active electro-optic components on-chip, which include the MRRs that modulate the incoming laser light with the error vector  $\mathbf{e}$  and the transimpedance amplifiers (TIAs) with tunable gain to convert photocurrent to voltage and scale it to implement the Hadamard product. To execute the DFA algorithm, a training example is first propagated through a neural network of variable

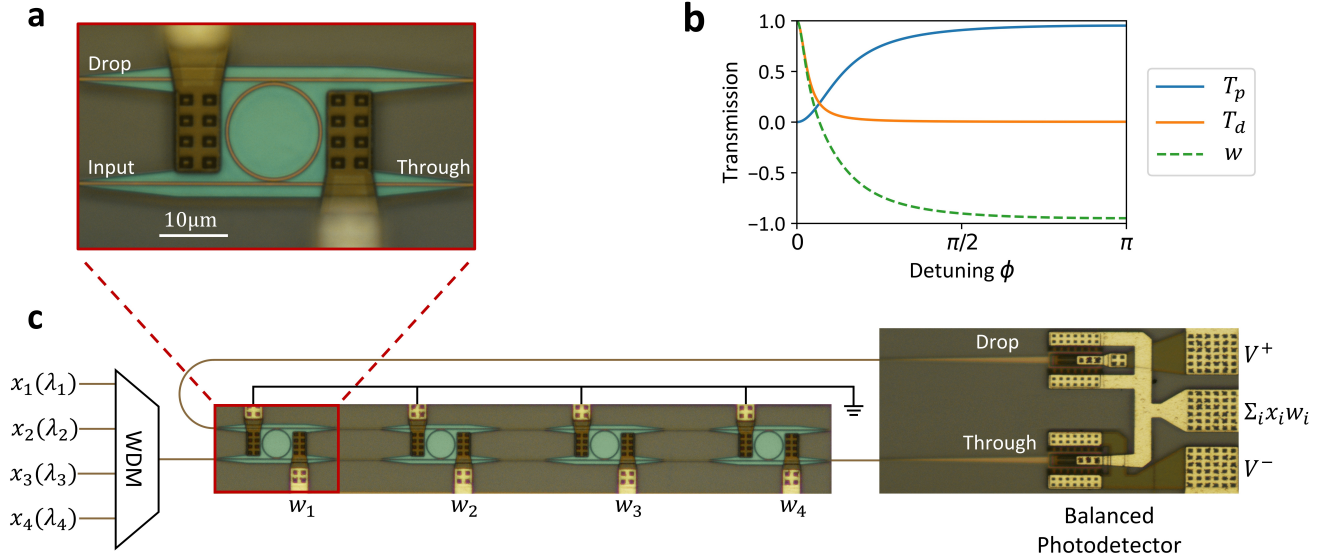


FIG. 2. **MAC operation and dot product with photonics.** (a) MRR in add-drop configuration with  $8\ \mu\text{m}$  radius coupled to through and drop ports. (b) Theoretical transmission profile of an add-drop MRR with a self-coupling coefficient of 0.95 and negligible attenuation. The weighting value  $w$  is given by  $T_d - T_p$ . (c) Array of four MRRs coupled to the through and drop ports which are connected to a balanced photodetector. The dot product operation is executed in the analog domain by injecting multi-channel analog signals with wavelength  $\lambda_i$  and amplitude  $x_i$ . Each MRR in the array is tuned to weight a corresponding wavelength by  $w_i$ , which yields the dot product  $\mathbf{x} \cdot \mathbf{w}$  in the electrical domain.

size. This inferencing operation can be performed using an analog photonic circuit<sup>13</sup> or with a separate digital processor. The error vector  $\mathbf{e}$  from the derivative of the cost function is then calculated using a dedicated CMOS processor that can be integrated on the chip. Finally, the electro-optic circuit calculates the DFA gradient vector  $\delta^{(k)}$  for each hidden layer  $k$ , which is used to update the network parameters.

To calculate the gradient vector  $\delta^{(k)}$  using the electro-optic circuit, WDM is used to combine  $N$  laser signals with different wavelengths onto a single waveguide. The element values in the error vector  $\mathbf{e}$  are amplitude encoded onto the  $N$  optical signals using an array of  $N$  all-pass MRRs, where each MRR is tuned for a corresponding optical wavelength. The intensities of the input optical signals are identical to allow an encoding scheme that linearly maps the amplitude modulation value to the through port transmission. The modulated optical signals representing the error vector  $\mathbf{e}$  are then coupled into arrays of parallel MRRs, herein referred to as the photonic weight bank, which perform the required matrix-vector product with the matrix  $\mathbf{B}^{(k)}$ .<sup>15</sup> The photonic weight bank consists of  $M$  rows of MRR arrays with  $N$  MRRs per row, where the incoming signals are coupled evenly into each row using  $1 \times M$  symmetrical optical splitters.<sup>29</sup> As discussed in the previous section for performing MAC operations in photonics, each MRR in the photonic weight bank is arranged in an add-drop configuration coupled to two separate waveguide buses connected to balanced photodetectors. To perform the matrix-vector product, each column of MRRs in the photonic weight bank is tuned for the corresponding optical wavelength  $\lambda_n$ , and thus the element  $B_{m,n}^{(k)}$  is mapped to the MRR in the  $m$ th row and  $n$ th column. Using the add-drop configuration, the incoming optical signals, which correspond to the error vector  $\mathbf{e}$ , are weighted by modifying the optical transmissions,  $T_p$  and  $T_d$ , for the through and drop ports of the MRRs. Summing the two transmission ports in the electrical domain allows the MRRs to be encoded with a weighting  $w \in [-1, 1]$ , assuming there is negligible loss in the system.<sup>30</sup> If the size of the photonic weight bank is larger than the dimensions of the matrix  $\mathbf{B}$ , the redundant MRRs can be tuned with a weighting of zero. A negative value in the error vector can be encoded in the architecture by inverting the sign of the inscribed weighting values of the corresponding column of MRRs in the photonic weight bank.

Finally, the Hadamard product between the two vectors  $\mathbf{B}^{(k)}\mathbf{e}$  and  $g'(\mathbf{a}^{(k)})$  is performed using a set of TIAs, where each balanced photodetector output is connected to a TIA. The vector  $g'(\mathbf{a}^{(k)})$  is calculated by the dedicated monolithic CMOS processor (the vector  $\mathbf{a}^{(k)}$  is known from the inference step) and encoded onto the voltage signals, supplied by the digital control system, that set the gain of the TIAs. The elements in the vector  $g'(\mathbf{a}^{(k)})$  are binary (0 or 1) when the ReLU activation function is employed. Since the vector  $\mathbf{a}^{(k)}$  was previously calculated during the forward inference process, setting the gain does not impede the system's maximum operating speed. The analog electrical signals are then converted to digital values with analog-to-digital converters (ADCs) and are used by the digital control system to update the neural network's weights.

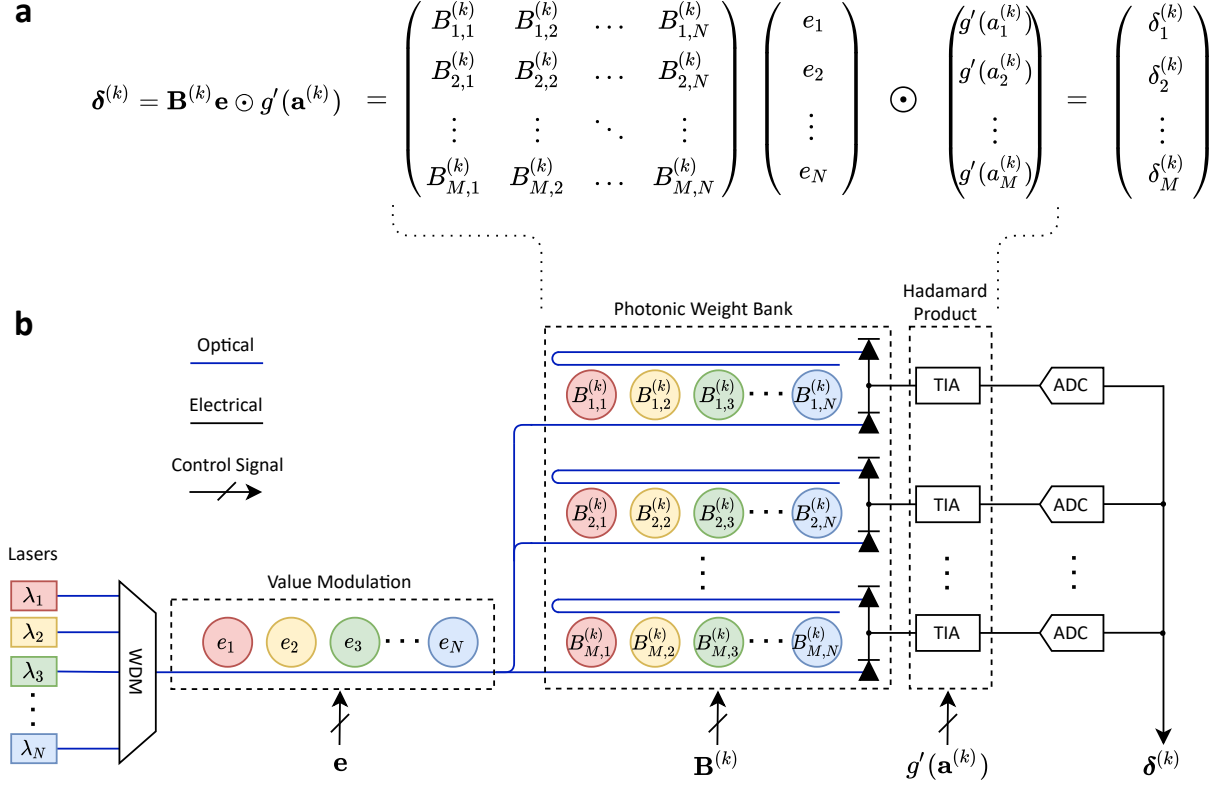


FIG. 3. **Photonic DFA architecture.** (a) Equation defining the gradient vector  $\boldsymbol{\delta}^{(k)}$  for the hidden layer  $k$ . (b) Silicon photonic architecture for calculating the gradient vector  $\boldsymbol{\delta}^{(k)}$  for the hidden layer  $k$ . The output layer gradient vector  $\mathbf{e}$  is amplitude encoded onto  $N$  different wavelengths using an array of MRRs, and the matrix-vector product of the  $M \times N$  matrix  $\mathbf{B}^{(k)}$  and vector  $\mathbf{e}$  is performed in the photonic weight bank. The Hadamard product between the vectors  $\mathbf{B}^{(k)}\mathbf{e}$  and  $g'(\mathbf{a}^{(k)})$  is executed using TIAs in the electrical domain, yielding the desired vector  $\boldsymbol{\delta}^{(k)}$  which is converted to the digital domain using ADCs. At each time step, the control signals that encode the MRRs and TIAs are fetched from memory.

The size of the photonic weight bank is physically bounded by the dimensions of the PIC and the maximum number of supported WDM channels in a single waveguide. The WDM channel limit is dependent on the finesse of the MRRs and the channel spacing, and an optimized design of the MRRs with a finesse of 368 could support up to 108 distinct channels.<sup>31</sup> However, the dimensions of the photonic weight bank do not restrict the size of the neural network being trained; if the size of the matrix  $\mathbf{B}^{(k)}$  is larger than the dimensions of the photonic weight bank, the product can be determined over multiple operational cycles by calculating a subset of the output vector at each cycle.

### DFA training experiment

In a proof-of-concept experiment to validate our proposed architecture, we collected experimental MRR operation data to train a feed-forward neural network with two hidden layers in a Python simulation using the MNIST dataset. We used an MRR with a radius of  $8\ \mu\text{m}$  (shown in Fig. 2a) which was fabricated on an SOI wafer with a silicon thickness of 220 nm and a buried oxide thickness of  $2\ \mu\text{m}$ . The MRR was thermally tuned using in-ring N-doped photoconductive heaters,<sup>28,32</sup> and was configured in an add-drop configuration which enabled the encoding of both positive and negative weighting values. The MRR was calibrated to determine the mapping between the applied bias and MRR weighting values, as described in the Methods section. The continuous optical signal injected into the MRR's input port was generated from an external cavity laser and was coupled into and out of the MRR using TE focusing grating couplers with a total loss of 12 dB. The input signal was modulated by a variable attenuator with 5 bits of precision, and the MRR tuning was controlled with 6 bits of precision using an applied bias voltage from a source meter.

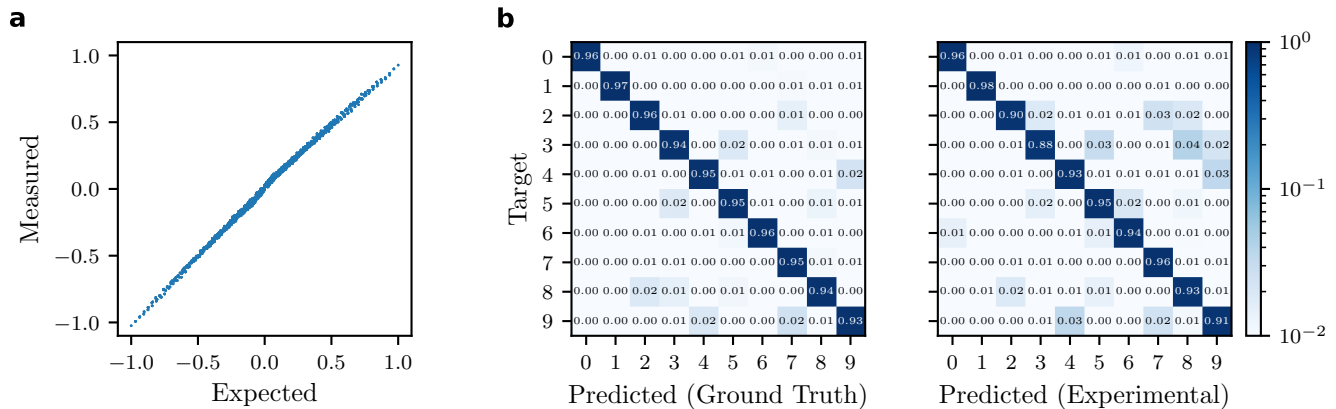


FIG. 4. **DFA on-chip training results.** (a) Experimental accuracy of MAC operations performed by an MRR. The error has a standard deviation of 0.019 and mean of 0.001. (b) Confusion matrices for feed-forward neural networks (2x800 ReLU) trained on the MNIST dataset using a standard CPU as the ground truth (95.11%) and experimental on-chip matrix-vector operation data (93.43%).

Multiplication operation data was collected by varying the encoded input signal and MRR weighting value while measuring the optical power in the drop and through ports,  $P_d$  and  $P_t$ , using a power meter. Following the photonic MAC scheme previously described, the multiplication result from the two operands (the input and MRR weighting value) was given by  $P_d - P_t$ . All possible non-redundant combinations of the input (5 bits) and weight (6 bits) values were measured three separate times during the data collection, and the average measurement was recorded. We then calibrated the optical power results to match the expected output range of values (-1 to 1) by performing a linear regression on the data, and the results are shown in Fig. 4a. The error from the experimental results, given by the expected product minus the measured data, has a standard deviation of 0.039 and a mean of 0.002.

The full photonic DFA architecture was simulated using a Python simulation that used the collected experimental results when performing the matrix-vector operations during the backward pass. We trained a  $784 \times 800 \times 800 \times 10$  feed-forward neural network with ReLU activation functions on the MNIST dataset, which was scaled between 0 and 1. We used the binary cross-entropy loss function, a constant learning rate of 0.003, and a mini-batch size of 64. The simulation achieved an accuracy of 93.43% using experimental data, which showed only a 1.68% drop (caused by error in the experimental multiplication operation data) from the results calculated entirely on a standard CPU as shown in Fig. 4b. The accuracy could be improved by implementing convolutional layers in the network, which have recently been demonstrated in photonics,<sup>30,33</sup> and by using an optimization algorithm such as RMSprop.<sup>34</sup>

### Energy and speed analysis

Matrix-vector multiplications are the fundamental operation performed during neural network training, and although they are a computationally expensive operation to perform in digital electronics, they can be executed in a single operational cycle in photonics. The power efficiency and speed of the photonic architecture are dependent on the size of the photonic weight bank and the maximum operational rate  $f_s$ , which is limited by the electronic device on-chip with the lowest throughput.<sup>30</sup> Defining an operation as either a multiplication or addition of two inputs, the maximum number of operations per second (OPS) computed by the photonic architecture scales linearly with the size of the weight bank ( $M \times N$ ) and is given by

$$\text{OPS} = 2f_s MN. \quad (2)$$

The lower bound on the required optical power per laser supplied to the photonic weight bank to overcome both the capacitance of the photodetectors with  $N_b$  bits of fixed precision and the shot noise is given by<sup>35</sup>

$$P_{\text{laser}} \geq M \frac{\hbar\omega}{\eta} \max \left( 2^{2N_b+1}, \frac{CV_d}{e} \right), \quad (3)$$

where  $\hbar\omega$  is the photon energy,  $\eta$  is the combined quantum efficiency of the laser, photodetector, and optical system loss through the waveguide,  $C$  and  $V_d$  are the capacitance and driving voltages of the photodetectors, and  $e$  is the elementary charge.

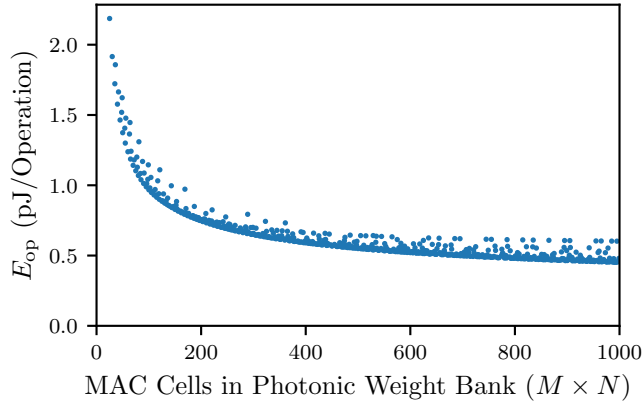


FIG. 5. The expected optimal energy per operation  $E_{op}$  as a function of the number of MAC cells in the photonic weight bank, where  $M, N \geq 5$ . The total energy consumption is dependent on both the number of MAC cells and the dimensions of the photonic weight bank, and only the lowest value of  $E_{op}$  as a function of the total number of MAC cells (i.e., the ideal photonic weight bank dimensions) is shown. The calculated values assume an operating speed of 12 GHz and 6 bits of precision.

During training, the tunable MRRs in the architecture are inscribed with a different value at each operational cycle. The values in the error vector  $\mathbf{e}$ , which can be stored in static random access memory (SRAM), are fetched and converted into analog voltage signals for tuning the designated MRRs using digital-to-analog converters (DACs). Unlike the dynamic  $\mathbf{e}$  vectors that change at each operational cycle, the inscribed weighting values of the MRRs in the photonic weight bank cycle through a set of known, unchanging values from the matrices  $\mathbf{B}^{(k)}$  for each hidden layer  $k$ . The control system for these MRRs can be made highly efficient by storing the set of weight values in an analog memory architecture, such as using resistive random access memory (RRAM) or optical memories based on phase change materials,<sup>36,37</sup> where the energy consumption required to access and switch between weights is negligible compared to the energy cost of modulating the input optical signals with the error vector. Thus, the estimated wall-plug power required by the DFA architecture with a photonic weight bank of size  $M \times N$  is given by

$$P_{\text{total}} = NP_{\text{laser}} + NP_{\text{DAC}} + N(M + 1)P_{\text{MRR}} + M(P_{\text{TIA}} + P_{\text{ADC}}). \quad (4)$$

The first term is the minimum required optical power, as shown in Eq. (3).<sup>35</sup> The second term accounts for the power required to convert the  $\mathbf{e}$  vector values into analog control signals using DACs ( $P_{\text{DAC}}$ ), and we assume that the energy required to fetch the data from the SRAM is negligible compared to the other components in the architecture.<sup>38</sup> The third term is the heating power required to tune the MRRs in the architecture ( $P_{\text{MRR}}$ ), and the final term corresponds to the power from the TIAs ( $P_{\text{TIA}}$ ) and ADCs ( $P_{\text{ADC}}$ ).

Using Eqs. (2) and (4), the expected optimal energy consumption per operation  $E_{op}$ , defined by  $P_{\text{total}}/\text{OPS}$ , as a function of the number of MAC cells in the photonic weight bank is shown in Fig. 5. To achieve an operational rate in the GHz range with low power consumption, our calculations assume the use of efficient, high speed MRRs with small footprints that are tuned using carrier depletion in an embedded reverse-biased p-n junction.<sup>39,40</sup> The power and performance speed of the photonic architecture were calculated assuming the use of the ReLU activation function and the following energy consumptions for the active electronic components: 190 mW per DAC (8 bit, 12 GS/s),<sup>41</sup> 13 mW per ADC (6 bit, 12.5 GS/s),<sup>42</sup> 2.4 pJ/bit per TIA (20 GS/s),<sup>43</sup> and a heating power of 5 mW per MRR.<sup>44</sup> The maximum operational rate  $f_s$  was limited by the throughput of the DAC to 12 GHz. We assumed an efficiency  $\eta$  of 0.2 for the laser source, photodetector, and optical system loss through the waveguide. The calculations assume the use of an optical signal with a wavelength of 1550 nm and high performance photodetector with a capacitance of 2.4 fF and a driving voltage of 1 V.<sup>33</sup> Using a photonic weight bank of size  $50 \times 20$ , we can achieve speeds of 24 teraoperations per second (TOPS) and an energy consumption  $E_{op}$  of 0.46 pJ per operation ( $<1$  pJ per MAC). The estimated compute density, defined by the OPS divided by the chip area, is 6.94 TOPS/mm<sup>2</sup>. We assume a photonic MAC cell of size  $47.4 \mu\text{m} \times 73.0 \mu\text{m}$ , which accounts for the overhead waveguide and electronic routing, bonding pads for MRR control, and sufficient spacing between MRRs to eliminate cross-talk (see Fig. 2a).

## DISCUSSION

The field of silicon photonics has rapidly accelerated over the last several years, however there exist a number of considerable challenges that must be addressed before the widespread adoption of optical technologies for AI

applications. Crucial for the calibration and control of the photonic components in our proposed architecture is the co-integration of active on-chip silicon electronics with silicon photonics.<sup>45</sup> Monolithic fabrication processes, which integrate electronics and photonics on the same substrate, are actively being investigated as the demand for silicon photonic technologies continues to grow. Recently, GlobalFoundries announced a dedicated homogeneous process that leverages state-of-the-art CMOS manufacturing with the integration of key photonic devices including SOI waveguides and germanium epitaxy photodetectors.<sup>46</sup> An alternative near-term implementation of the photonic architecture could use flip-chip bonding by fabricating two dies and soldering them together, where one is optimized for the silicon photonics components and the other for the CMOS electronics. This flip-chip bonding approach does not require the development of new manufacturing processes and can use existing designs for the electronic components (microprocessors, SRAM, signal converters, etc.).

Another challenge facing silicon photonic computational architectures is their current reliance on off-chip light sources connected through fiber packaging. Several recent approaches have been proposed to integrate light sources directly onto silicon waveguide layers, including strain engineering of germanium and all-silicon emissive defects and rare-earth-element doping.<sup>47,48</sup> An alternative approach, which is well suited for our highly-parallelized photonic architecture, is the use of an on-chip frequency comb source that generates evenly spaced emission wavelengths.<sup>49</sup> The use of an on-chip frequency comb source has recently been experimentally demonstrated for performing photonic in-memory computing.<sup>33</sup> However, the optical source must be capable of producing enough optical power for the entire system, which includes the requirement to overcome the capacitance and shot noise of the photodetectors, and must also be efficient.

In summary, we have designed a silicon photonic architecture that executes the fundamental operations of the DFA algorithm in the analog domain, including matrix-vector multiplication and the Hadamard product, to calculate the gradient vector of each neural network layer in situ. The architecture is cascadable for training neural networks of various sizes. Using a photonic weight bank of size  $50 \times 20$ , the system is expected to perform up to 24 TOPS while consuming less than 1 pJ per MAC operation. The expected improvements in training time and energy efficiency offered by this photonic architecture could enable the development of innovative neural network applications that would be impossible to operate on current generation hardware. Future work includes demonstrating a complete integrated system, which includes a dedicated CMOS processor, that is capable of operating at high speeds to train neural networks without requiring any data processing off-chip.

## METHODS

### Experimental photonic hardware operation

The experimental operation of our photonic hardware requires a control system that consists of both source and power meters. The source meters provide heating currents to the MRRs, which shift their resonances using the thermo-optic effect. The power meters monitor the output from the drop and through ports ( $T_d$  and  $T_p$ ). The source and power meters must be calibrated by creating a mapping from their output analog values to their expected encoded values in the photonic system.

Initially, the resonances of the MRR were determined through a wavelength sweep using a tunable laser. The mapping between the applied current and MRR weight value were then found by performing a sweep of the applied current while providing a constant laser source and measuring the optical response. The MRR mapping was found to be accurate to 6 bits of precision. The multiplication data was then obtained by measuring all possible combinations of weight values and injected input signals which were modulated off-chip using an attenuator with 5 bits of precision. The product of these two values was represented as the power difference between the drop and through ports of the MRR,  $T_d - T_p$ . A linear regression on the power difference values was then performed to reduce the error when mapping the experimental results to the range of desired digital values, which was between -1 and 1.

### Direct feedback alignment algorithm

In feedforward neural networks, the nodes are clustered in different layers where the signals can only pass from a preceding to a succeeding layer. The behaviour of all nodes in an ANN is identical: the input signals from the preceding layer are weighted and summed, and a non-linear activation function is applied to the sum which is outputted to all the nodes in the succeeding layer. The forward propagation of the input signal using trained weights is known as inferencing. The inference of an ANN with  $l$  layers can be described mathematically for each layer  $k$  (defining



TABLE I. Machine learning notation used in this paper.

Symbol	Description
$\mathbf{W}^{(k)}$	Weight matrix between layers $k$ and $k - 1$
$\mathbf{b}^{(k)}$	Bias vector between layers $k$ and $k - 1$
$\mathbf{a}^{(k)}$	Sum of the weighted input signals in the layer $k$
$g(\mathbf{a}^{(k)})$	Activation function of the neurons in the layer $k$
$\mathbf{h}^{(k)}$	Activation of the nodes in the layer $k$
$\mathbf{x}$	Training input
$\mathbf{y}$	Target output
$\hat{\mathbf{y}}$	Output of neural network from training input $\mathbf{x}$
$J(\mathbf{x}, \mathbf{y}, \boldsymbol{\theta})$	Cost function
$\boldsymbol{\theta}$	Network parameters including weights and biases
$\mathbf{e}$	Error from gradient of the cost function

$\mathbf{h}^{(0)} \equiv \mathbf{x}$ ) as

$$\mathbf{a}^{(k)} = \mathbf{W}^{(k)} \mathbf{h}^{(k-1)} + \mathbf{b}^{(k)}, \quad (5)$$

$$\mathbf{h}^{(k)} = g(\mathbf{a}^{(k)}), \quad (6)$$

where the variables used are defined in Table I.

Feedforward neural networks approximate a function  $f$  by defining a mapping  $\hat{\mathbf{y}} = f(\mathbf{x}; \boldsymbol{\theta})$ , and the goal of training is to find the values of the network parameters  $\boldsymbol{\theta} = \{\mathbf{W}, \mathbf{b}\}$  that reduce the overall error between the actual and target outputs.<sup>50</sup> The error to be minimized can be expressed as a cost function  $J(\mathbf{x}, \mathbf{y}, \boldsymbol{\theta})$ , where  $\mathbf{y}$  is the target output and the choice of cost function depends on the specific application of the neural network.

The DFA algorithm first determines the gradient of the cost function in the output layer  $l$ , which is the error propagated to the hidden layers:

$$\mathbf{e} = \nabla_{\mathbf{a}^{(l)}} J(\mathbf{x}, \mathbf{y}, \boldsymbol{\theta}) = \nabla_{\mathbf{h}^{(l)}} J(\mathbf{x}, \mathbf{y}, \boldsymbol{\theta}) \odot g'(\mathbf{a}^{(l)}), \quad (7)$$

where  $\odot$  is the Hadamard product (element-wise multiplication operator) and  $g'$  is the derivative of the activation function with respect to  $\mathbf{a}^{(l)}$ . The DFA algorithm calculates the gradients for each hidden layer  $k$  as

$$\boldsymbol{\delta}^{(k)} = \mathbf{B}^{(k)} \mathbf{e} \odot g'(\mathbf{a}^{(k)}), \quad (8)$$

where  $\mathbf{B}^{(k)}$  is a fixed random weight matrix with appropriate dimensions.

Using the gradients calculated in Eqs. 7 and 8 and defining  $\boldsymbol{\delta}^{(l)} \equiv \mathbf{e}$ , the update functions of the network parameters  $\boldsymbol{\theta}$  for each layer  $k$ , ignoring the learning rate, are

$$\nabla_{\mathbf{b}^{(k)}} J(\mathbf{x}, \mathbf{y}, \boldsymbol{\theta}) = \boldsymbol{\delta}^{(k)}, \quad (9)$$

$$\nabla_{\mathbf{W}^{(k)}} J(\mathbf{x}, \mathbf{y}, \boldsymbol{\theta}) = \mathbf{h}^{(k-1)} \boldsymbol{\delta}^{(k)}. \quad (10)$$

The deep learning algorithm stochastic gradient descent can be implemented to improve training performance. A minibatch of examples  $\mathbb{B} = \{\mathbf{x}_1, \dots, \mathbf{x}_m\}$  of size  $m$  from the training set are used to compute the update functions found in Eqs. 9 and 10.<sup>50</sup> The update value for each parameter is then averaged from the minibatch calculations and the network parameters are updated by following the estimated gradient downhill:

$$\boldsymbol{\theta} \leftarrow \boldsymbol{\theta} - \frac{\alpha}{m} \sum_{i=1}^m \nabla_{\boldsymbol{\theta}} J(\mathbf{x}_i, \mathbf{y}_i, \boldsymbol{\theta}), \quad (11)$$

where  $\alpha$  is the learning rate. The training procedure for updating the network parameters is repeated until the required network accuracy is satisfied.

#### DATA AVAILABILITY

The data that support the findings of this study are available from the corresponding author upon reasonable request.

## REFERENCES

- [1] LeCun, Y., Bengio, Y. & Hinton, G. Deep learning. *Nature* **521**, 436–444 (2015).
- [2] Schuman, C. D. *et al.* A survey of neuromorphic computing and neural networks in hardware. Preprint at <https://arxiv.org/abs/1705.06963> (2017).
- [3] Von Neumann, J. First draft of a report on the EDVAC. *IEEE Ann. Hist. Comput.* **15**, 27–75 (1993).
- [4] Mead, C. Neuromorphic electronic systems. *Proc. IEEE* **78**, 1629–1636 (1990).
- [5] Amodei, D. & Hernandez, D. AI and compute. Blog at <https://openai.com/blog/ai-and-compute> (2018).
- [6] Canziani, A., Paszke, A. & Culurciello, E. An analysis of deep neural network models for practical applications. Preprint at <http://arxiv.org/abs/1605.07678> (2017).
- [7] Shastri, B. J. *et al.* Photonics for artificial intelligence and neuromorphic computing. *Nat. Photonics* **15**, 102–114 (2021).
- [8] Prucnal, P. R. & Shastri, B. J. *Neuromorphic Photonics* (CRC Press, 2017).
- [9] Chrostowski, L. & Hochberg, M. *Silicon Photonics Design* (Cambridge University Press, 2015).
- [10] Hochberg, M. *et al.* Silicon photonics: The next fabless semiconductor industry. *IEEE J. Solid-State Circuits* **5**, 48–58 (2013).
- [11] de Lima, T. F. *et al.* Machine learning with neuromorphic photonics. *J. Light. Technol.* **37**, 1515–1534 (2019).
- [12] Peng, H.-T., Nahmias, M. A., de Lima, T. F., Tait, A. N. & Shastri, B. J. Neuromorphic photonic integrated circuits. *IEEE J. Sel. Top. Quantum Electron.* **24**, 1–15 (2018).
- [13] Tait, A. N. *et al.* Neuromorphic photonic networks using silicon photonic weight banks. *Sci. Rep.* **7**, 7430 (2017).
- [14] Shen, Y. *et al.* Deep learning with coherent nanophotonic circuits. *Nat. Photonics* **11**, 441–446 (2017).
- [15] Tait, A. N. *et al.* Silicon photonic modulator neuron. *Phys. Rev. Appl.* **11**, 064043 (2019).
- [16] Zuo, Y. *et al.* All-optical neural network with nonlinear activation functions. *Optica* **6**, 1132–1137 (2019).
- [17] Esser, S. K. *et al.* Convolutional networks for fast, energy-efficient neuromorphic computing. *Proc. National Academy of Sciences* **113**, 11441–11446 (2016).
- [18] Strubell, E., Ganesh, A. & McCallum, A. Energy and policy considerations for deep learning in NLP. *Proc. Annual Meeting of the Association for Computational Linguistics*, 3645–3650 (2019).
- [19] Rumelhart, D. E., Hinton, G. E. & Williams, R. J. Learning representations by back-propagating errors. *Nature* **323**, 533–536 (1986).
- [20] Nøkland, A. Direct feedback alignment provides learning in deep neural networks. *Proc. Advances in Neural Information Processing Systems* **29**, 1037–1045 (2016).
- [21] Launay, J., Poli, I., Boniface, F. & Krzakala, F. Direct feedback alignment scales to modern deep learning tasks and architectures. *Proc. Advances in Neural Information Processing Systems* **33**, 9346–9360 (2020).
- [22] Refinetti, M., D’Ascoli, S., Ohana, R. & Goldt, S. Align, then memorise: the dynamics of learning with feedback alignment. *Proc. International Conference on Machine Learning*, 8925–8935 (2021).
- [23] Bogaerts, W. *et al.* Silicon microring resonators. *Laser Photonics Rev.* **6**, 47–73 (2012).
- [24] Reed, G. T., Mashanovich, G., Gardes, F. Y. & Thomson, D. J. Silicon optical modulators. *Nat. Photonics* **4**, 518–526 (2010).
- [25] Tait, A. N. *et al.* Microring weight banks. *IEEE J. Sel. Top. Quantum Electron.* **22**, 312–325 (2016).
- [26] Zhang, W. *et al.* Microring weight banks control beyond 8.5-bits accuracy. Preprint at <http://arxiv.org/abs/2104.01164> (2021).
- [27] Tait, A. N. *et al.* Feedback control for microring weight banks. *Opt. Express* **26**, 26422 (2018).
- [28] Jayatilaka, H., Shoman, H., Chrostowski, L. & Shekhar, S. Photoconductive heaters enable control of large-scale silicon photonic ring resonator circuits. *Optica* **6**, 84–91 (2019).
- [29] T., S., S., I. G. & M., R. Design and analysis of 1xN symmetrical optical splitters for photonic integrated circuits. *Optik* **169**, 321–331 (2018).
- [30] Bangari, V. *et al.* Digital electronics and analog photonics for convolutional neural networks (DEAP-CNNs). *IEEE J. Sel. Top. Quantum Electron.* **26**, 1–13 (2020).
- [31] Tait, A. N. Silicon Photonic Neural Networks (Doctoral Dissertation, Princeton University, 2018).
- [32] Jayatilaka, H. *et al.* Wavelength tuning and stabilization of microring-based filters using silicon in-resonator photoconductive heaters. *Opt. Express* **23**, 25084–25097 (2015).
- [33] Feldmann, J. *et al.* Parallel convolutional processing using an integrated photonic tensor core. *Nature* **589**, 52–58 (2021).
- [34] Tieleman, T. & Hinton, G. Lecture 6.5–RmsProp: Divide the gradient by a running average of its recent magnitude. *COURSERA: Neural networks for machine learning* (2012).
- [35] Nahmias, M. A. *et al.* Photonic multiply-accumulate operations for neural networks. *IEEE J. Sel. Top. Quantum Electron.* **26**, 1–18 (2020).
- [36] Zahoor, F., Azni Zulkifli, T. Z. & Khanday, F. A. Resistive random access memory (RRAM): an overview of materials, switching mechanism, performance, multilevel cell (mlc) storage, modeling, and applications. *Nanoscale Res. Lett.* **15**, 90 (2020).
- [37] Miscuglio, M. *et al.* Artificial synapse with mnemonic functionality using GSST-based photonic integrated memory. *Proc. 2020 International Applied Computational Electromagnetics Society Symposium (ACES)*, 1–3 (2020).
- [38] Boumchedda, R. *et al.* 1.45-fJ/bit access two-port SRAM interfacing a synchronous/asynchronous IoT platform for energy-efficient normally off applications. *IEEE Solid-State Circuits Lett.* **1**, 186–189 (2018).
- [39] Dong, P. *et al.* Wavelength-tunable silicon microring modulator. *Opt. Express* **18**, 10941 (2010).

- [40] Pantouvaki, M. *et al.* 56Gb/s ring modulator on a 300mm silicon photonics platform. *Proc. 2015 European Conference on Optical Communication (ECOC)*, 1–3 (2015).
- [41] Savoj, J., Abbasfar, A., Amirkhany, A., Jeeradit, M. & Garlepp, B. W. A 12-GS/s phase-calibrated CMOS digital-to-analog converter for backplane communications. *IEEE J. Solid-State Circuits* **43**, 1207–1216 (2008).
- [42] Alphacore. ADC (Analog-to-Digital converter) A6B12G.
- [43] Lee, Y. & Chen, W. A 20-Gb/s, 2.4 pJ/bit, fully integrated optical receiver with a baud-rate clock and data recovery. In *2018 IEEE International Symposium on Circuits and Systems (ISCAS)*, 1–4 (2018).
- [44] Peng, H.-T., Nahmias, M. A., de Lima, T. F., Tait, A. N. & Shastri, B. J. Neuromorphic photonic integrated circuits. *IEEE J. Sel. Top. Quantum Electron.* **24**, 1–15 (2018).
- [45] Bogaerts, W. & Chrostowski, L. Silicon photonics circuit design: Methods, tools and challenges. *Laser Photonics Rev.* **12**, 1700237 (2018).
- [46] Giewont, K. *et al.* 300-mm monolithic silicon photonics foundry technology. *IEEE J. Sel. Top. Quantum Electron.* **25**, 1–11 (2019).
- [47] Buckley, S. *et al.* All-silicon light-emitting diodes waveguide-integrated with superconducting single-photon detectors. *Appl. Phys. Lett.* **111**, 141101 (2017).
- [48] Zhou, Z., Yin, B. & Michel, J. On-chip light sources for silicon photonics. *Light Sci. Appl.* **4**, e358–e358 (2015).
- [49] Gaeta, A. L., Lipson, M. & Kippenberg, T. J. Photonic-chip-based frequency combs. *Nat. Photonics* **13**, 158–169 (2019).
- [50] Goodfellow, I., Bengio, Y. & Courville, A. *Deep Learning* (MIT Press, 2016).

### ACKNOWLEDGEMENTS

This research is supported by the Natural Sciences and Engineering Research Council of Canada (NSERC) and the Vector Scholarship in Artificial Intelligence, provided through the Vector Institute.

### AUTHOR CONTRIBUTIONS

M.F. and B.S. conceived the idea. Z.G., H.M., and B.M. designed and conducted the experiments. M.F. created the Python simulation. M.F., M.A., and S.S. analyzed the data. V.S., P.P., and B.S. supervised the research and contributed to the general concept and interpretation of the results. All authors discussed the results and contributed to the manuscript.

### COMPETING INTERESTS

The authors declare no competing interests.